Conduction Velocities of Excitatory Axons Innervating Parvalbumin Interneurons in Primary Somatosensory Cortex

Kate Scheuer[1]

Xinyu Zhao[2,3]

Meyer Jackson[3]

1. Cellular and Molecular Biology Program, 2. Waisman Center, and 3. Department of Neuroscience, University of Wisconsin-Madison, Madison, Wisconsin 53705

Corresponding author email: meyer.jackson@wisc.edu

Conflict of interest statement: The authors declare no competing financial or non-financial interests.

Acknowledgements: National Institutes of Health Grants NS105200 and NS093866 to M.B.J. and X.Z. Thanks to Dr. Shane McMahon for methodological contributions.

Abstract

Timing plays a critical role in signaling throughout the nervous system. Signaling times vary widely depending on distance and speed, and timing delays influence circuit computations such as coincidence detection, synaptic integration, entrainment, temporal summation, and plasticity. Parvalbumin (PV) interneurons are a major type of inhibitory neuron with critical roles throughout the brain. Their rapid-spiking characteristics enable them to control the dynamics of neural circuits across a range of time scales. However, little is known about the factors that determine the timing of their synaptic inputs. Here, we measured the conduction velocity (CV) of excitatory axons that target PV interneurons in mouse primary somatosensory cortex. Using a genetically-encoded hybrid voltage sensor (hVOS) targeted to PV interneurons, we clocked the arrival of excitatory synaptic inputs with sub-millisecond precision in large numbers of cells across multiple layers. Arrival times varied with distance, allowing us to determine the CV of the excitatory axons. Values ranged from 28–241 μm/msec across layers 2-5, and interlaminar CV was about twice as fast as intralaminar CV. This will enable more rapid computation within columns, while integration between columns will be slower. hVOS imaging from specific cell types offers a unique opportunity to investigate conduction in axons defined by their targets.

Introduction

Axonal conduction velocity (CV) influences neural computations by controlling the timing of synaptic inputs. CV impacts processes such as coincidence detection, temporal summation, entrainment, oscillations, synaptic integration, and synaptic plasticity (Bucher & Goaillard, 2011; Chomiak, Peters, & Hu, 2008; Fields, 2015; Pajevic, Basser, & Fields, 2014; Salami, Itami, Tsumoto, & Kimura, 2003). Small variations in CV can have a profound impact on synchrony and oscillation frequency (Ivanov, Polykretis, & Michmizos, 2019; Pajevic et al., 2014), and CV alterations have been linked to a variety of diseases including diabetes (Candy & Szatkowski, 2000), schizophrenia (Corcoba et al., 2015), and Down Syndrome (Olmos-Serrano et al., 2016). Demyelination associated with degenerative diseases such as multiple sclerosis has a major impact on CV (Compston & Coles, 2002; Nave, 2010; Pedroni, Minh do, Mallamaci, & Cherubini, 2014), and slower CV caused by decreased erbB signaling has been linked to bipolar disorder and schizophrenia (Roy et al., 2007).

CV is determined by axonal diameter and other geometric properties, as well as the capacitance and intrinsic excitability of the axonal membrane. CV varies widely between different axons and functional pathways. Axons projecting from ventral temporal cortex to the inferior colliculus conduct approximately three times faster than those projecting to caudate putamen (Chomiak et al., 2008), and hippocampal dentate granule cell (mossy fiber) axons conduct more rapidly than the axons of hilar mossy cells (Ma, Bayguinov, & Jackson, 2017). CV can also differ within the axons of the same cell. For a given ventral temporal cortical neuron, axonal branches with contralateral targets have significantly slower CV compared to axonal branches with ipsilateral targets (Chomiak et al., 2008). CV may also vary based on postsynaptic cell type. As a result of differences in CV, stimulating the same thalamic neuron activates

inhibitory targets before excitatory targets in somatosensory barrel cortex (BC), thus setting a very narrow time window for excitation (Kimura et al., 2010). Additionally, cell type can influence CV variability. Martinotti cells in layer 5 (L5) BC have more variable axonal CVs compared to pyramidal cells in the same layer (Shlosberg, Abu-Ghanem, & Amitai, 2008). These many variations in CV determine not only computation speed, but by influencing timing and delays, determine how circuits encode and process information.

Previous measurements of CV have been hindered by technical constraints arising from the difficulty of recording directly from axons, as well as low throughput, and lack of spatial and temporal resolution. Voltage imaging has provided a powerful general method for the measurement of axonal CV (Grinvald, Ross, & Farber, 1981; Hamada, Popovic, & Kole, 2017; Popovic, Foust, McCormick, & Zecevic, 2011; Sakai et al., 1991), and genetically-encoded voltage indicators have extended the approach to these problems through the addition of targeting specificity (Ma, Bayguinov, & Jackson, 2019; Panzera & Hoppa, 2019). The hybrid voltage sensor (hVOS) has sub-millisecond temporal resolution, single-cell spatial resolution (Chanda et al., 2005; Ghitani, Bayguinov, Ma, & Jackson, 2015; Ma et al., 2017), and can be targeted to specific cell populations (Bayguinov, Ma, Gao, Zhao, & Jackson, 2017; Chanda et al., 2005; Ghitani, Bayguinov, Ma, & Jackson, 2015; Ma et al., 2017). hVOS reveals voltage changes from large numbers of neurons simultaneously, and when targeted directly to axons, can resolve differences in CV based on cell type (Ma et al., 2017). In this study, we used hVOS to measure CV along excitatory axons targeting inhibitory parvalbumin (PV) interneurons in mouse BC. Because they fire rapidly and have a short membrane time constant, PV interneurons play a critical role in controlling the temporal integration window of their targets (Cardin, 2018; Ferguson & Gao, 2018; Galarreta & Hestrin, 2002; Pouille & Scanziani, 2001). They are also

essential for the generation of gamma oscillations, rhythmic brain waves between 30 and 80 Hz which affect sensory integration, working memory, social cognition, and other functions (Gandal, Edgar, Klook, & Siegel, 2012; Gloveli et al., 2005; Gonzalez-Burgos, Cho, & Lewis, 2015; Pouille & Scanziani, 2001). Both PV interneurons and gamma oscillations have been implicated in a variety of psychiatric and neurological disorders including schizophrenia, bipolar disorder, and autism spectrum disorder (Gonzalez-Burgos et al., 2015; Lauber, Filice, & Schwaller, 2018; T. Y. Liu et al., 2012). The fast-spiking behavior of PV interneurons suggests that they are adapted to rapid computations. Thus, the speed of their activation by excitatory inputs is likely to be important to their function.

While PV interneurons are present throughout L2-6, their density and circuitry vary widely within the cortex (Staiger & Petersen, 2021). Properties such as excitation/inhibition balance and gamma oscillation frequency, both linked to PV interneuron function, differ based on cortical layer (Adesnik, 2018; Xu et al., 2016). We used the response latencies of PV interneurons to determine CV within and between different cortical layers. CV varied widely from 44 ± 15 μm/msec (mean ± SD) for L2/3 intralaminar CV to up to 241 μm/msec for L5 → L4 CV. The mean interlaminar CV (111 ± 49 μm/msec) was about twice as fast as the mean intralaminar CV (57 ± 41 μm/msec). These differences between inter- and intralaminar CV will influence processing within the BC to make computations within columns faster than computations between columns.

Results

PV interneuron responses to stimulation in L2/3, L4, and L5

In mice from PV-Cre crosses with hVOS Cre reporter mice (see Methods), hVOS probe has been shown to be expressed in 83% of PV interneurons with 99.2% specificity (Bayguinov et al., 2017). In slices from these mice, BC cortical layers and barrels are visible in gradient contrast optics (Fig. 3A) and fluorescence (Fig. 3B; note that the images were taken with different cameras, so the fields of view do not align precisely). Layers were identified by cell density and cell size (Feldmeyer, 2012; Woolsey & Van der Loos, 1970), and boundaries between layers are marked with dashed lines (Figs. 1, 3, 4, Supp. Fig. 1). Fields of view generally contained L2/3 through L5 (Fig. 1). Barrels were separated into faint "hollows" (Feldmeyer, 2012; Woolsey & Van der Loos, 1970) as well as stronger fluorescence in L4, and boundaries between columns marked by dotted lines (Fig. 3, 4, Supp. Fig. 1). Electrical stimulation in L2/3, L4, and L5 elicited voltage changes in PV interneurons distributed through L2-5, as shown in the maximum amplitude heatmaps in Figs. 1A (L2/3), 1B (L4), and 1C (L5). Warmer colors correspond to greater changes in fluorescence and indicate the presence of responsive PV interneurons. Traces from locations (indicated by number and color) reveal corresponding variations in the magnitude of PV interneuron depolarization (Fig. 1D-F). Dark blue regions of the heatmap indicate the absence of responsive PV interneurons, and traces from those locations show no discernable stimulus-evoked fluorescence change.

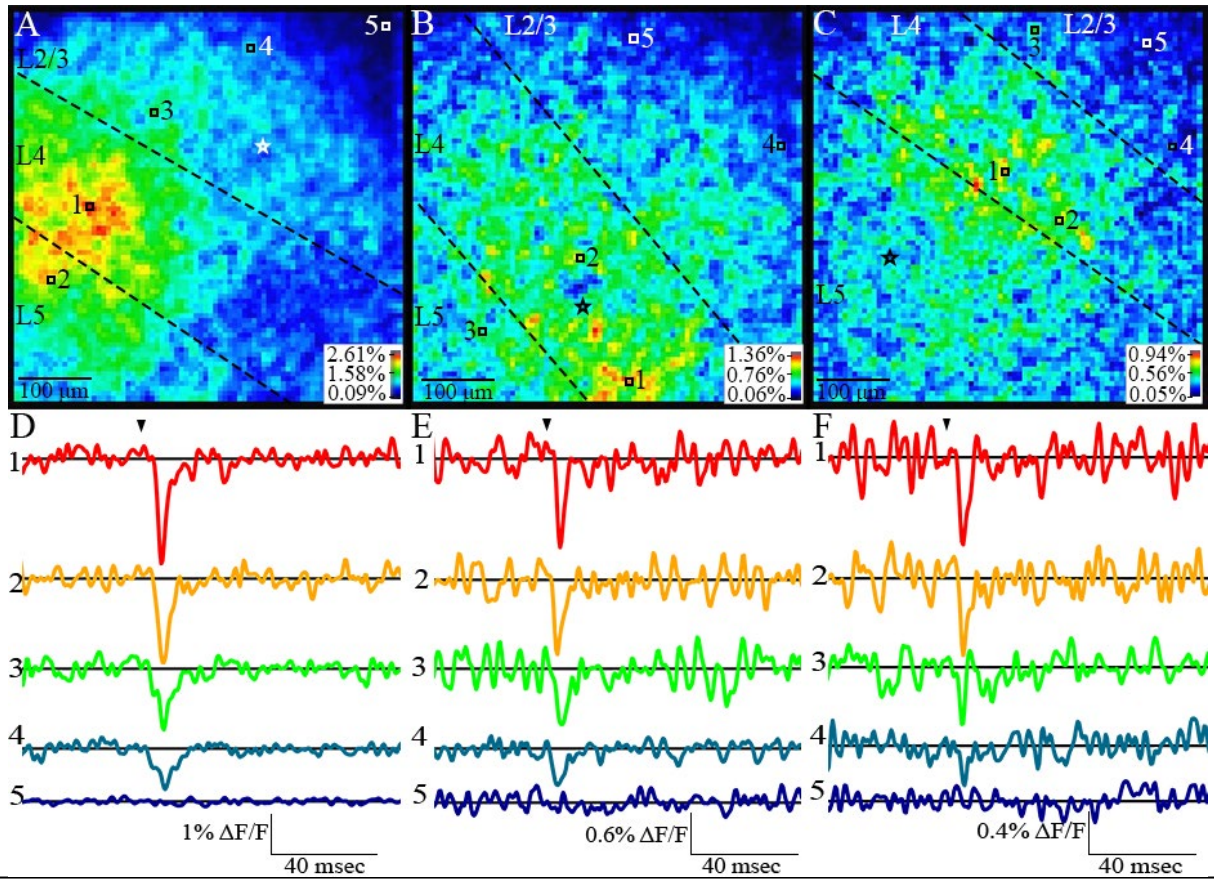

Figure 1. PV interneurons throughout a slice respond to stimulation in L2/3 (A), L4 (B), L5 (C) (stimulation sites indicated by white or black stars). In maximum amplitude heatmaps, warmer colors indicate greater changes in fluorescence. These differences in amplitude are visible in selected traces of fluorescence versus time (D-F) from the corresponding heatmaps above. Locations of traces are indicated with small white or black squares and numbers in each map. Arrowheads indicate time of stimulation.

Stronger stimulation elicited responses in more cells over greater distances. Heatmaps of signal-to-noise ratio (SNR) revealed that stimulation with 10 µA rarely elicited detectable responses (Fig. 2A). Increasing the stimulus current to 20 µA (Fig. 2B) and 60 µA (Fig. 2C) elicited responses in more neurons over greater distances, and increasing to 100 µA depolarized still more neurons over a broader range of distances encompassing nearly the entire field of view (Figs. 1, 2D). Responses depended on synaptic excitation, as they were blocked by 10 µM NBQX (Figs. 2E-2F). Patterns of response spread varied but often included intralaminar responses across multiple barrel columns (Video 1) and/or interlaminar responses within and between barrel columns (Videos 2, 3). These excitatory responses spread away from the stimulus

electrode as action potentials propagated along excitatory efferents; the speed of this spread reflects the CV along these axons.

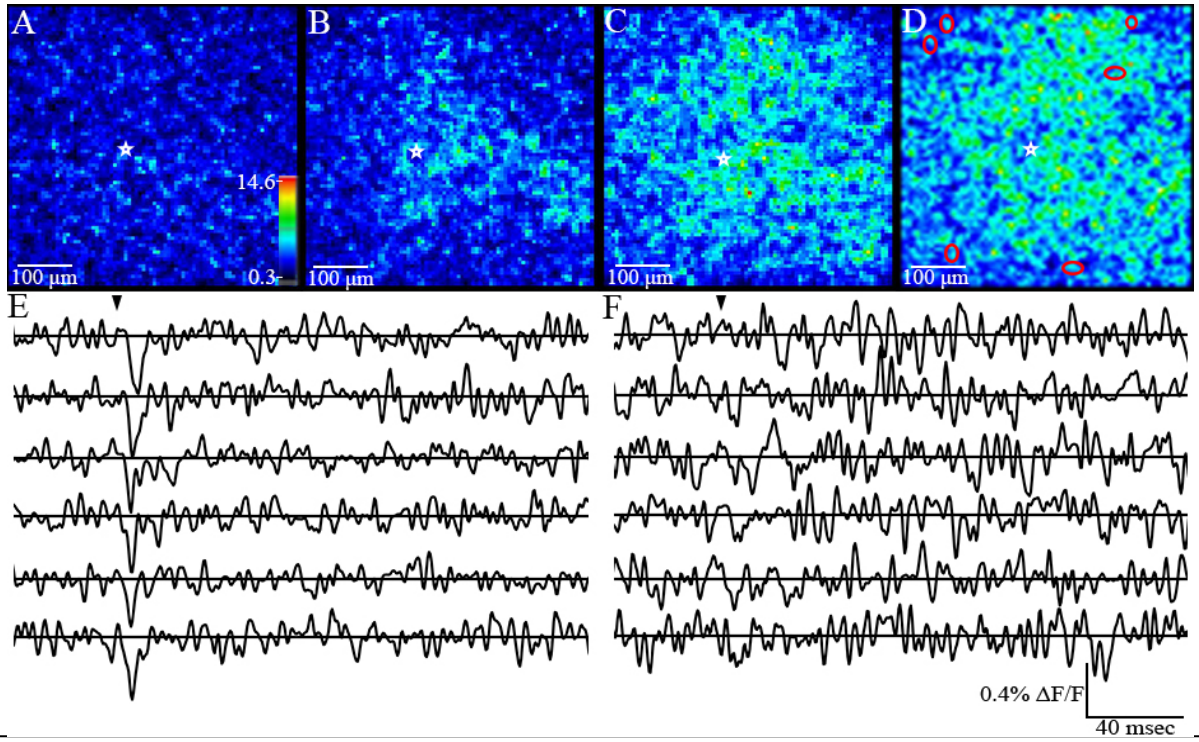

Figure 2. PV interneuron responses to different stimulation currents. Heatmaps of SNR following stimulations of 10 µA (A), 20 µA (B), 60 µA (C), and 100 µA (D). Site of stimulation is marked with a white star in A-D. Heatmap scale in (A) also applies to (B-D). A method of analysis was developed to identify individual, non-overlapping cells with clear responses (see Methods for criteria). E-F. Traces from 6 clearly identified PV interneurons (circled in red in D) show fluorescence versus time before (E) and after (F) the addition of 10 µM NBQX. Blockade by NBQX indicates that responses are glutamatergic.

Identification of single PV interneurons

Determining CV requires the observation of responses in significant numbers of clearly identified neurons with well-resolved locations and accurately measured latencies. Fluorescence images of slices (Fig. 3B) display diffusely distributed fluorescence due to the dense arborization of PV interneurons (Fukuda & Kosaka, 2003). This makes it difficult to locate individual cells precisely. This, together with the large numbers of responsive cells, made manual analysis extremely time-consuming. We therefore developed a semi-automated method to identify responsive PV interneurons (see Methods and Supp. Fig. 1). Briefly, pixels above a baseline SNR cutoff (Supp. Fig. 1A) were divided into groups using k-means clustering of the SNR maps

(Supp. Fig. 1B). Putative somata were identified as contiguous groups of pixels in the same k-means cluster based on the reasoning that pixels from the same cell body are expected to have a similar SNR. A pixel group was considered to be a PV interneuron soma if its amplitude and SNR were above the cutoffs (0.1% for amplitude, 5 for SNR), did not share a face with another pixel group, and was < 20 μm across (consistent with the size of a PV interneuron soma (Kooijmans, Sierhuis, Self, & Roelfsema, 2020; Selby, Zhang, & Sun, 2007; Y. Wang, Gupta, Toledo-Rodriguez, Wu, & Markram, 2002)).

This process provided a reproducible, robust method of identifying individual PV interneurons free of subjective choices. The procedure is illustrated with a slice from which a gradient contrast image is shown in Fig. 3A and a resting fluorescence image is shown in Fig. 3B. The electrode, visible in L2/3 in both images, was used to apply a stimulation of 100 μA. A SNR heatmap revealed activated cells concentrated in L4, but cells in L2/3 and L5 also responded (Fig. 3C). This heatmap highlights 56 PV interneurons identified with our clustering method. Responsive neurons were outlined in black, or in red for locations selected for display of fluorescence versus time (Fig. 3D). The 8 selected traces show clear depolarizing responses following stimulation.

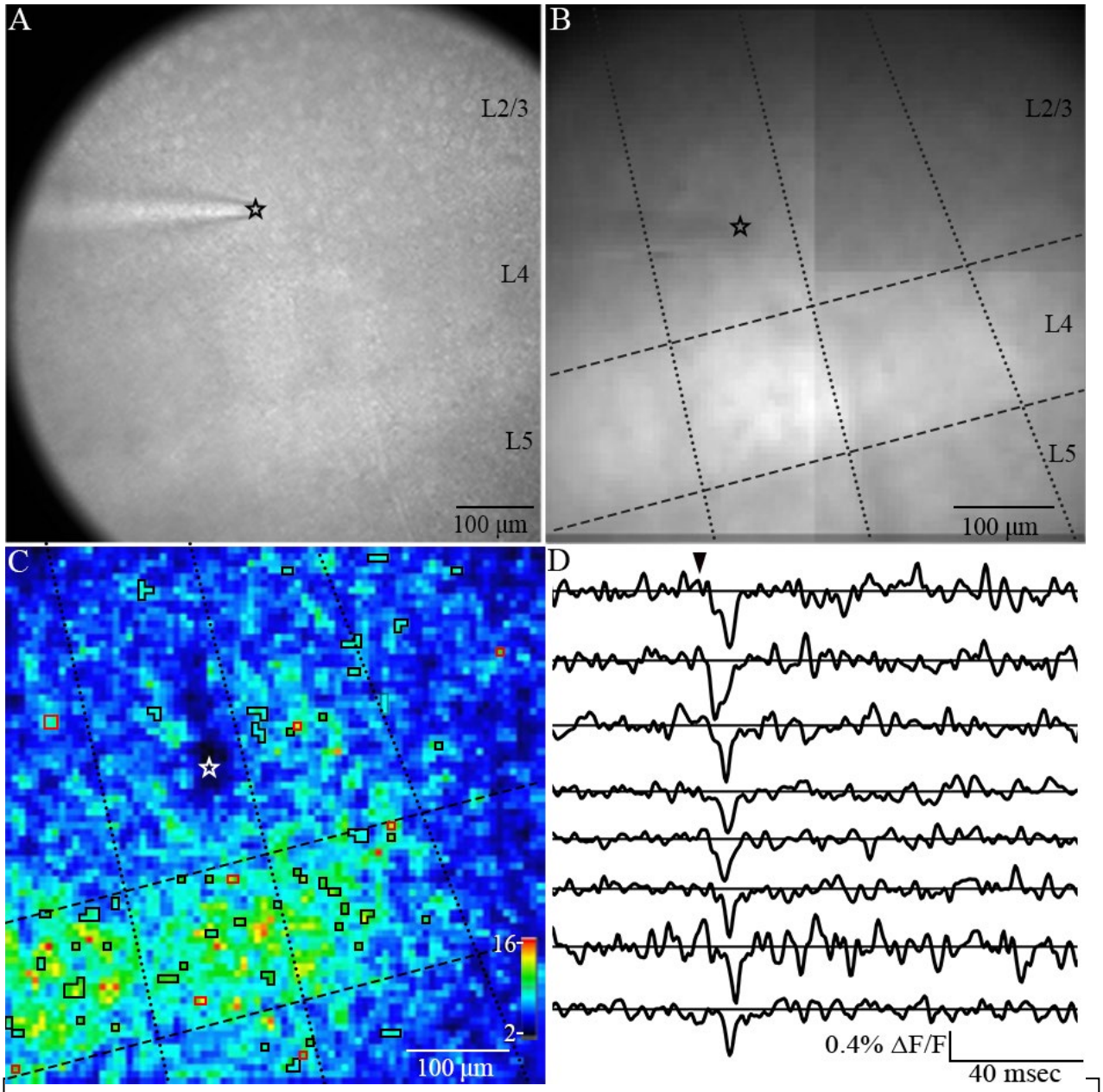

Figure 3. Identification of responsive PV interneurons. A. Gradient contrast image (taken with the Kiralux camera), and B. fluorescence image (taken with the CCD-SMQ camera) of a BC somatosensory cortical slice containing L2/3, L4 and L5. The stimulating electrode is visible in L2/3 (star at the tip, black in A and B, white in C). Layer boundaries are indicated by dashed lines, and barrel column borders are indicated with dotted lines in B-C. Following 100 µA stimulation, responsive PV interneurons were identified based on K-means clustering of SNR and other criteria (see Methods and Supp. Fig. 1). C. A SNR heatmap shows that responsive PV interneurons span the field of view and are present in L2-5. We identified 56 responsive PV interneurons outlined in black or red. D. Traces of fluorescence versus time for the 8 PV interneurons outlined in red in C. Arrowhead above indicates stimulation time. All displayed traces show clear decreases in fluorescence following stimulation, indicating depolarization of the highlighted PV interneurons.

Returning to Fig. 2, this method identified 12, 96, 176, and 115 responsive PV interneurons for 10, 20, 60, and 100 µA stimulation, respectively. The decrease in number of

identifiable cells with 100 μA reflects the higher proportion of overlapping cells that could not be disambiguated. The best balance between extensive spread with large numbers of readily resolved individual cells versus too much overlap was seen with 100 μA, so this stimulus strength was used for experiments on CV. The broad patterns of propagation are clearly evident in unprocessed data as illustrated in the heatmaps and supplemental videos described above. However, by employing method we were able to focus on somata and improve the precision of latency determination. We were thus able to analyze large numbers of cells over a broad area with a wide range of propagation distances. This analysis thus provided a robust identification of responsive neurons and, together with our choice of experimental conditions, optimized the determination of CV.

Intra- and interlaminar conduction velocity

As an action potential propagates along the axon of an excitatory neuron, PV interneurons closer to the site of initiation respond first and those farther away respond later (Fig. 4A). A sequence of frames taken at one msec intervals from 2 msec to 6 msec after stimulation illustrate the spatiotemporal pattern of response spread (Fig. 4B). Note that these frames represent the SNR at successive time points, compared to the maps in Figs. 1-3 showing the maximum value within the entire post-stimulus measure window. The frames in Fig. 4B show that PV interneuron responses occur first mostly nearer the stimulating electrode in L4 (2-3 msec), spread vertically both ways to L2/3 and L5 (4-5 msec), and then spread both vertically and horizontally through L2/3 and L5 (5-6 msec). Thus, a single experiment can capture propagation along different populations of axons, and because fields of view contained large numbers of responsive neurons (typically ~50-100), we were generally able to identify 8 or more neurons along distinct trajectories to track propagation. Fig. 4C-D presents resting fluorescence

and maximum SNR maps, respectively, showing the locations of responsive cells along one selected trajectory (L4 → L2/3 CV). A plot of latency versus distance fitted to a line gave us the CV as inverse of the slope (Fig. 4E). By constructing plots along different trajectories, we determined the CV of different subpopulations of axons that target PV interneurons. Focusing on PV interneurons in the same layer as the stimulation electrode (between dashed lines in Fig. 4B-D) provided a determination of intralaminar (horizontal) CV, and focusing on PV interneurons in the same barrel column as the stimulating electrode (between dotted lines in Fig. 4B-D) provided a determination of interlaminar (vertical) CV. Interlaminar CV often included an additional neighboring barrel column. This is consistent with results from rat BC indicating that excitatory axons tend to project within the same and/or neighboring columns but usually not to columns beyond the nearest neighbor (Narayanan et al., 2015).

In 22 out of 59 slices, plots of latency versus distance had statistically significant correlations. Among the remaining slices, negative correlations occurred only rarely (4 out of 59 slices). The highest CV we were able to measure was 241 μm/msec (19 PV interneurons), and nearly half (15) of the experiments without significant positive correlations yielded CV values above the highest measurable value. In these cases, the spread within the field of view was too fast to detect differences in latency. In most cases of such rapid propagation, latencies varied by less than 0.5 msec (average root-mean-square error = 0.427). These results indicate that in many slices, the CV was faster than can be measured over the distances accessible within our field of view. In the remainder of this work, we will focus primarily on CV measurements with significant distance-latency correlations, unless stated otherwise, and recognize that this biases our analysis uniformly toward slower conduction.

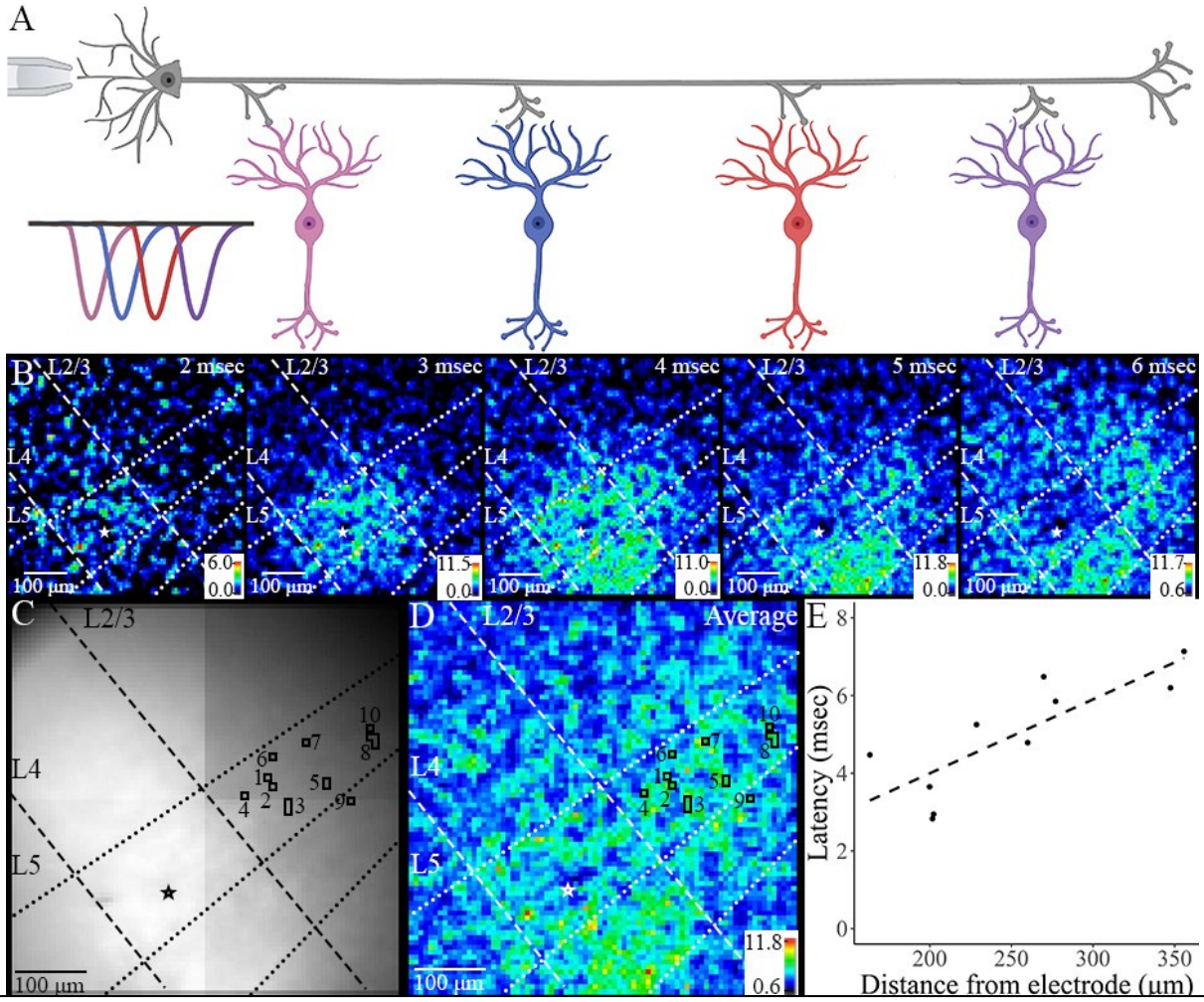

Figure 4. A. Stimulation excites principal cells, their axons, or both (gray). As an action potential propagates along an excitatory axon, synapses on PV neurons evoke sequential responses (pink, blue, red, purple). (Created with BioRender; https://biorender.com). B. Sequential responses can be observed in a sequence of SNR heatmaps at one msec intervals (times after stimulation indicated in the top right corner of each frame). PV interneuron responses occur first mostly near the stimulating electrode in L4 (2-3 msec), and spread vertically and horizontally through the slice. A white start indicates the site of stimulation in all frames (See videos in supplemental data). Resting fluorescence image (C) and average SNR response heatmap within a 20 msec measure window (D). Black (C) or white (D) stars indicate site of stimulation. Dashed lines mark layer boundaries (B-D). Dotted black (C) or white (B, D) lines perpendicular to layer boundaries outline the stimulated and neighboring barrel. Ten responsive PV interneurons identified by our grouping method along an L4 → L2/3 CV trajectory are outlined in black in C and D, with numbers indicating response order. E. Latency plotted versus distance for these 10 cells. The relationship between latency and distance was significant (t = 4.255, p-value = 0.004), and the slope yielded a CV of 51 µm/msec.

Stimulation in L2/3, L4, and L5 elicited responses that spread within those layers, and latency versus distance plots yielded intralaminar CV values in L2/3 and L5. In L4 the lack of correlation prevented us from determining the CV (N=3), and this may indicate that intralaminar

211 conduction is faster in this layer. L2/3 intralaminar CV measurements were generally slow with
212 low variance (44 ± 15 μm/msec, N = 52 PV interneurons from 4 slices). The two measured L5
213 intralaminar CV values were very different (28 μm/msec and 136 μm/msec, N = 18 PV
214 interneurons from 2 slices), potentially reflecting differences between L5 pyramidal cell
215 subtypes, which are known to vary in target projection layers and morphology (Larsen &
216 Callaway, 2006). Fig. 5A shows a plot of latency versus distance with an intralaminar CV in
217 L2/3 of 37 μm/msec (t = 4.86, p = 0.0009).

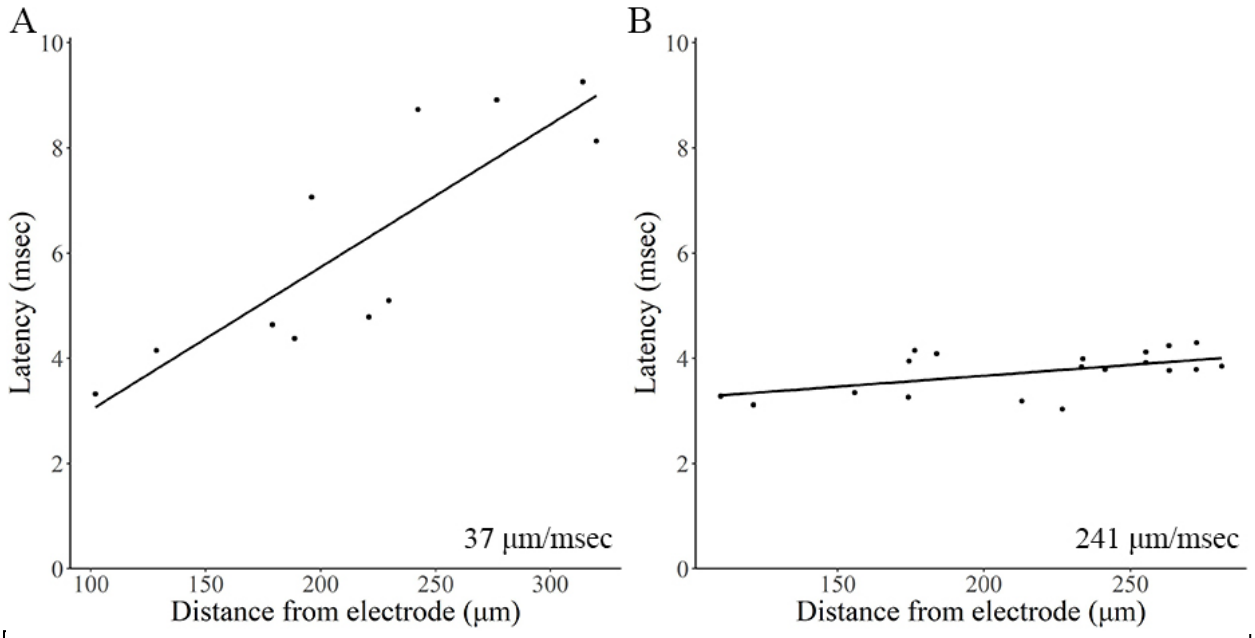

Figure 5. Latency versus intralaminar (A) or interlaminar (B) distance for two representative experiments. The steeper slope in A compared to B indicates that the L2/3 intralaminar CV represented in A (37 μm/msec) is slower than the L5 → L4 interlaminar CV shown in B (241 μm/msec).

218 Correlated latency-distance plots for interlaminar propagation were obtained for all pairs
219 of layers with the exception of L5 → L2/3. Fig. 5B shows a plot for L5 → L4 conduction
220 yielding a CV of 241 μm/msec (t = 2.63, p = 0.018). For three other pairs of layers CV values
221 were similar to one another, with L4 → L2/3 giving CV = 94 ± 37 μm/msec (N = 62 PV
222 interneurons, 3 slices), L5 → L2/3 giving CV = 107 ± 48 μm/msec (N = 57 PV interneurons, 3
223 slices), and L2/3 → L4 giving CV = 81 ± 36 μm/msec (N = 93 PV interneurons, 5 slices). Faster

CV values were obtained for L4 → L5 (144 μm/msec, N = 8 PV interneurons, 1 slice) and L5 → L4 (154 ± 58 μm/msec, N = 63 PV interneurons, 4 slices), including our fastest CV of 241 μm/msec (Fig. 5B). The plot of latency versus distance for L5 → L4 in Fig. 5B is noticeably less steep than the plot of L2/3 intralaminar CV in Fig. 5A, supporting the view that the L5 → L4 CV is faster than the intralaminar CV.

Interlaminar CVs (111 ± 49 μm/msec, N = 16 slices) were about twice as fast as intralaminar CVs (57 ± 41 μm/msec, N = 6 slices), and this difference was statistically significant ($t = -2.587$, $p = 0.026$, Fig. 6A). This difference remained significant even excluding the single particularly fast interlaminar CV value of 241 μm/msec ($t = -2.352$, $p = 0.046$). ANOVA followed by post-hoc testing revealed that intralaminar CV is about 2.7 times slower than L5 → L4 interlaminar CV (Fig. 6B, ANOVA: $F = 3.085$, $p = 0.046$; Tukey's honestly significant differences: L5 → L4 CV versus intralaminar CV: $p = 0.025$). Including values for slices with CVs too fast to produce significant correlations further supports the assertion that interlaminar CV is faster than intralaminar CV. This increased the number of intralaminar CV measurements by 50% (N = 3 additional slices) but increased the number of interlaminar CV measurements by 75% (N = 12 additional slices). Interestingly, one of these three additional intralaminar CV values was from L4, possibly suggesting faster intralaminar CV in L4 than L2/3 or L5. Because a higher proportion of interlaminar CV values were too fast to measure, our focus on experiments with statistically significant correlations underestimates the difference between interlaminar and intralaminar CV.

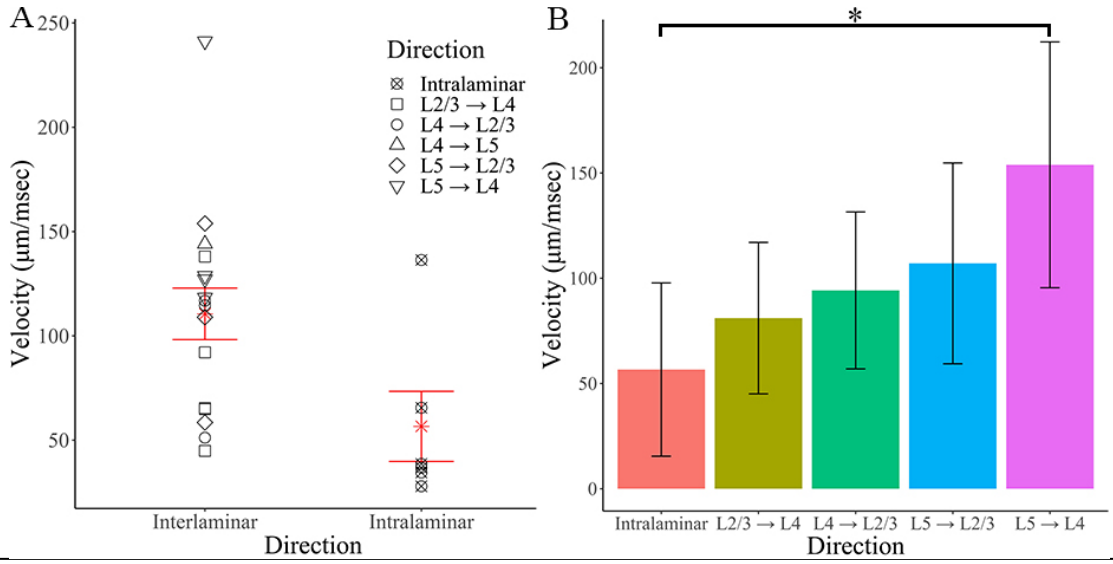

Figure 6. Inter- and intralaminar CV. A. Interlaminar CV (111 ± 49 µm/msec) is approximately twice as fast as intralaminar CV (57 ± 41 µm/msec; t = -2.587, p = 0.026). Symbol shapes indicate CV direction (in legend), and group mean ± SD are shown in red. B. Intralaminar (70 PV interneurons, 6 slices), L2/3 → L4 (93 PV interneurons, 5 slices), L4 → L2/3 (62 PV interneurons, 3 slices), L5 → L2/3 (57 PV interneurons , 3 slices), and L5 → L4 (63 PV interneurons, 4 slices) CV. Error bars indicate SD. CV varies significantly based on direction (F = 3.085, p = 0.046), and intralaminar CV is significantly slower than L5 → L4 CV (p= 0.025).

Discussion

Action potential conduction influences virtually all aspects of neural circuit function, and many approaches have been taken to measure its velocity. Antidromic activation (Chomiak et al., 2008; Palmer & Stuart, 2006; Salami, Itami, et al., 2003; Shlosberg et al., 2008), whole-cell recording (Chomiak et al., 2008; Helmstaedter, Staiger, Sakmann, & Feldmeyer, 2008; Kim, Renden, & von Gersdorff, 2013; Kimura et al., 2010; McDougall et al., 2018; Salami, Itami, et al., 2003; Salami, Kimura, & Tsumoto, 2003; Shlosberg et al., 2008; Shu, Duque, Yu, Haider, & McCormick, 2007) and voltage-sensitive dye imaging (Grinvald et al., 1981; Hamada et al., 2017; Popovic et al., 2011; Sakai et al., 1991) provide accurate measurements of CV but are limited by their low-throughput and lack of specificity. Other methods lack spatial resolution and are poorly suited to investigations of single-cell responses (Candy & Szatkowski, 2000; Drakesmith et al., 2019; Emmenegger, Obien, Franke, & Hierlemann, 2019; Kress & Mennerick, 2009; Radivojevic et al., 2017; Salami, Kimura, et al., 2003). The present study used the

genetically-encoded voltage sensor hVOS to measure CV of excitatory axons targeting PV interneurons in mouse BC. Because it can be genetically targeted, hVOS provides a unique opportunity to measure CV along axons innervating specific cell types. hVOS imaging has a rapid response time that is well-suited for measuring the sub-millisecond differences in latency required for the determination of CV. Although DPA increases membrane capacitance and thus slows propagation, this effect is small as increasing DPA from 2 to 4 µM reduced CV by only 15% in mossy fibers (Ma et al., 2017). Furthermore, this uniform effect will reduce CV proportionally in different populations of axons. In the present study it was difficult to measure faster CV values, but this could be remedied by reducing magnification to track conduction over longer distances. Our analysis has incorporated the assumption that axons follow a direct path to target PV interneurons at different distances. This adds to the biases that reduce our estimates of CV. This is probably more important for interlaminar than intralaminar conduction, as interlaminar axons sometimes extend vertically through cortical layers before branching horizontally (Larsen & Callaway, 2006; Schubert, Kotter, Luhmann, & Staiger, 2006).

CV values reported here are somewhat slower than in previous studies, which can probably be attributed to our exclusion of experiments without a significant correlation between latency and distance. Including these experiments yielded a value of 304 ± 501 µm/msec (N = 670 PV interneurons from 37 slices), which trends toward the higher end of the range from previous reports. Prior studies reported CV values of 140-160 µm/msec in mouse anterior cingulate cortex (Lee, Miao, Chen, Li, & Zhuo, 2021), 150-550 µm/msec in rat visual cortex (Murakoshi, Guo, & Ichinose, 1993), 161-240 µm/msec in rat CA3 (Soleng, Raastad, & Andersen, 2003), about 200-300 µm/msec in mouse BC (Shlosberg et al., 2008), 200 µm/msec in rat BC (Helmstaedter et al., 2008), and 340 µm/msec in rat primary somatosensory cortex

(Telfeian & Connors, 2003). While some of the variations in these studies can be attributed to methodological differences such as temperature, this wide range of CV values probably also reflects the diversity of cortical axons. Axonal diameter, varicosity geometry, and myelination vary widely and all have a major impact on CV. Ion channel expression also varies widely between cell types and compartments (Liu, Wang, Pitt, & Liu, 2022; Vacher, Mohapatra, & Trimmer, 2008), and by controlling the intrinsic excitability of the axonal membrane will have an impact on CV. Our measurements of CV values for different projections in the same preparation offer a perspective to the variations between prior reports, and support the view that this quantity can vary between axons in the same brain region.

PV interneuron microcircuitry, density, and excitation/inhibition input ratios differ between cortical layers (Adesnik, 2018; Staiger & Petersen, 2021; Xu et al., 2016), and the CV of axons innervating different PV interneurons will impact their function in cortical microcircuits. The canonical cortical circuit for information flow begins with thalamic inputs to L4 followed by transmission to L2/3 and then L5. We could follow this flow to measure a CV of 94 ± 37 μm/msec along L4 excitatory axons targeting L2/3 PV interneurons. We also report CV along excitatory axons following noncanonical circuits. For example, L2/3 receives input from L5 (Narayanan et al., 2015; Staiger & Petersen, 2021; Thomson, West, Wang, & Bannister, 2002; Vecchia et al., 2020), and for this projection we measured a CV of 107 ± 48 μm/msec, which was similar to the L4 → L2/3 CV. We also measured CV along axons from L2/3 and L5 to L4 PV interneurons. Although most L2/3 excitatory cells project to infragranular or supragranular cortical layers, a small portion target L4 PV interneurons (Thomson et al., 2002), including a subset of L2/3 pyramidal cells with somata near the L3/4 border (Larsen & Callaway, 2006). Our L2/3 → L4 CV of 81 ± 36 μm/msec was slightly slower than other interlaminar CVs.

There is also evidence for monosynaptic L5 excitatory cell coupling to L4 fast-spiking interneurons (Vecchia et al., 2020), and our CV in this direction of 154 ± 58 μm/msec was particularly rapid. These non-canonical pathways targeting L4 PV interneurons may influence feedback to L4 and therefore impact integration of intracortical and incoming ventral posteromedial thalamic input. Intralaminar spread was observed in L2/3, L4, and L5. The very slow L2/3 intralaminar CV value reported here of 44 ± 15 μm/msec is consistent with reported values of 33-60 μm/msec for intralaminar spread of population excitatory responses in this layer (Petersen, Grinvald, & Sakmann, 2003).

Interestingly, we found the average intralaminar CV (of L2/3 and L5) to be about twice as slow as the average interlaminar CV (Fig. 6A) and approximately 2.7 times slower than the interlaminar L5 → L4 CV (Fig. 6B). These differences have important implications for cortical function. Long, horizontal L2/3 pyramidal cell axons have been previously observed in multiple cortical areas across species (Bruno, Hahn, Wallace, de Kock, & Sakmann, 2009; Gilbert, 1992; Gottlieb & Keller, 1997; Keller & Asanuma, 1993; McGuire, Gilbert, Rivlin, & Wiesel, 1991). These projections are thought to connect cortical areas with similar functions, such as visual regions with similar orientation selectivity (Gilbert, 1992). In BC, L2/3 pyramidal cell intralaminar axons tend to extend across barrels corresponding to whisker rows rather than arcs, possibly reflecting a directional preference (Feldmeyer, 2012). Both regular-spiking and fast-spiking units, putative pyramidal cells and PV interneurons, respectively, show selectivity to whisking direction in BC L2/3 (Andermann & Moore, 2006; Kremer, Leger, Goodman, Brette, & Bourdieu, 2011). Our measurement of L2/3 intralaminar CV may reflect the targeting of the PV interneurons of these domains. Murine L5 intralaminar excitatory projections connect multiple barrel columns (Schubert et al., 2006; Schubert et al., 2001), and intralaminar excitatory

inputs to L5 pyramidal cells usually extend across one and a half barrel columns, so L5 pyramidal cells may integrate information from three whiskers. Thus, the L5 intralaminar CV is likely to impact multi-whisker integration. While L5 → L4 axonal projections are uncommon (Staiger & Petersen, 2021), optogenetic stimulation of L5 pyramidal cells elicits firing in L4 fast-spiking interneurons, and inhibition of L5 pyramidal cells lengthens the reaction time in a texture discrimination test (Vecchia et al., 2020). L5 → L4 CV may therefore impact temporal sharpness of responses to sensory stimuli. Together, these results suggest that interlaminar cortical circuits process more rapidly than intralaminar circuits. Thus, precise timing of inputs to PV interneurons is likely to play an important role in computations performed within a cortical column and to be less critical in the collective computations performed by multiple columns. The higher CV for interlaminar conduction than intralaminar conduction found in the present study will thus meet distinct demands of different forms of cortical computation.

hVOS imaging offers a new and powerful approach to the study of CV, not only in the axons of defined cell types (Ma et al., 2017), but also in the axons defined by their targeted cell types. An important example of such specificity is that thalamocortical projections to inhibitory neurons have a faster CV than projections to excitatory cells, allowing interlaminar inhibition to activate L4 targets prior to L2/3 targets (Kimura et al., 2010). Targeting hVOS probes to different types of neurons has the potential to reveal many additional forms of axon specialization adapted to different forms of neuronal computation.

Materials and Methods

Animals

Ai35-hVOS1.5 (C57BL/6-*Gt(ROSA)26Sor*$^{tm1(CAG\text{-}hVOS1.5)Mbja}$/J, JAX 031102) Cre reporter mice (Bayguinov et al., 2017) were bred with PV Cre driver mice (B6.129P2-Pvalb$^{tm1(cre)Arbr}$/J, JAX 017320) to create animals with PV interneuron-specific hVOS probe expression. All animal procedures were approved by the Animal Care and Use Committee of the University of Wisconsin-Madison School of Medicine and Public Health (ACUC protocol: M005952).

Hybrid voltage sensor (hVOS)

The hVOS probe used here harbors a cerulean fluorescent protein (CeFP) tethered to the inner cell membrane by a truncated h-ras motif (Wang, Zhang, Chanda, & Jackson, 2010). Slices are perfused with 4 μM dipicrylamine (DPA), a small anion which partitions into the cell membrane. Membrane depolarization drives DPA towards the CeFP to quench fluorescence through Förster resonance energy transfer. Repolarization drives the DPA away allowing fluorescence to return to baseline (Chanda et al., 2005; Wang et al., 2010). Fluorescence thus reports voltage changes selectively from PV interneurons because these cells express the probe with very high specificity (Bayguinov et al., 2017). DPA has a time resolution < 0.5 msec (Bradley, Luo, Otis, & DiGregorio, 2009; Chanda et al., 2005) and tracks action potentials with excellent temporal fidelity (Ghitani et al., 2015; Ma et al., 2019). Parameters such as latency, amplitude, and half-width were determined from traces of fluorescence versus time (Fig. 7). Amplitude was taken as the peak change in fluorescence from the pre-stimulus baseline, and half-width as the time between rise and fall at half-maximal response. Latency is the time from stimulation to half-maximal response.

Slice preparation

371 Four- to ten-week-old male and female mice were deeply anesthetized with isoflurane
372 and sacrificed via cervical dislocation. Brains were dissected and placed into ice-cold cutting
373 solution (in mM: 10 glucose, 125 NaCl, 4 KCl, 1.25 NaH_2PO_4, 26 $NaHCO_3$, 6 $MgSO_4$, 1 $CaCl_2$)
374 bubbled with 95% O_2/5% CO_2. Coronal slices (300 µm) were prepared using a Leica VT1200S
375 vibratome and placed into artificial cerebrospinal fluid (ACSF, same as cutting solution except
376 1.3 mM $MgSO_4$, 2.5 mM $CaCl_2$, and 4 µM DPA) and bubbled with 95% O_2/5% CO_2 for at least
377 one hour.

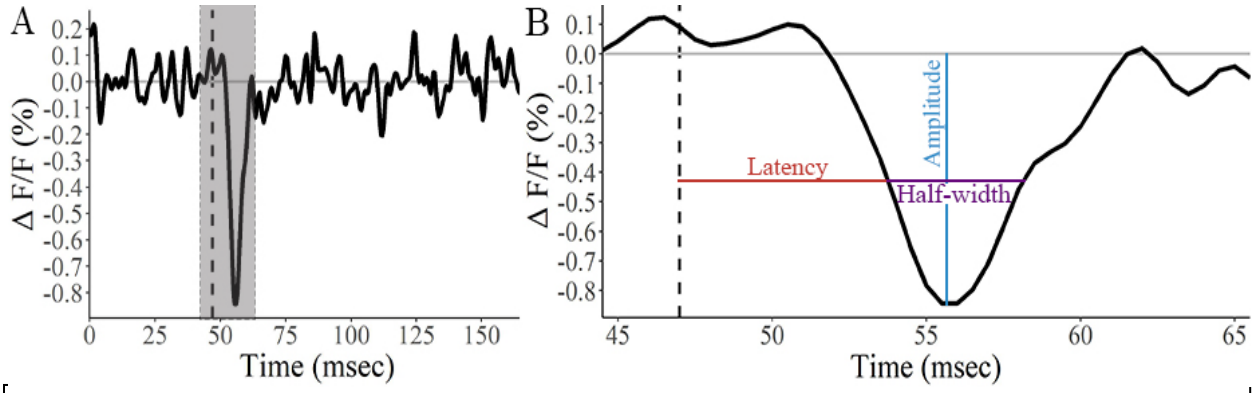

Figure 7. PV interneuron electrical activity was recorded as fluorescence using a genetically-encoded hybrid voltage sensor (hVOS). A. PV interneuron response parameters are extracted from traces of fluorescence versus time. Gray shading indicates the 20 msec measurement window expanded in B. B. Amplitude is the maximum change in fluorescence from baseline. Half-width is the time between half-maximal change in fluorescence during the rising and decay phases. Latency is the time from stimulation to half-maximal change in fluorescence of the rising phase.

378 *Voltage imaging*

379 Slices were continuously perfused with ACSF at room temperature and viewed using a
380 BX51 Olympus microscope. Layer and barrel boundaries were visually identified based on both
381 fluorescence and gradient contrast images (Feldmeyer, 2012; Woolsey & Van der Loos, 1970).
382 Stimulus pulses (100 µA, 180-µsec, except Fig. 2A-C which used 10-60 µA) were generated by a
383 stimulus isolator (World Precision Instruments, Sarasota, Florida) and applied to various
384 locations within BC with fire-polished, ACSF-filled KG-33 glass electrodes (King Precision
385 Glass, Claremont, California) with tip diameter ~6-8 µm. Traces of fluorescence versus time
386 were averages of 15-30 trials. Slices were illuminated with 435 nm light using an LED light

source (Prizmatix, Holon, Israel). Gradient contrast images were acquired with a Kiralux (Thorlabs, Newton, New Jersey) CMOS camera; fluorescent images were acquired with this camera for better visualization, but for voltage imaging we used a CCD-SMQ camera (RedShirt Imaging, Decatur, Georgia) at a framerate of 2000 Hz and 80x80 spatial resolution. Data were acquired with a custom data acquisition and analysis program that controlled stimulation and illumination (Chang, 2006).

Data processing and analysis

Fluorescence divided by resting light intensity ($\Delta F/F$) was passed through a nine-point binomial temporal filter and a spatial filter with $\sigma = 1$. A polynomial baseline correction was calculated using fluorescence outside of a 20 msec measurement window from 2 msec before to 18 msec after the stimulus. Parameters including amplitude, half-width, and latency were calculated from traces of fluorescence versus time. Heatmaps showing SNR are each normalized to the maximum value within the field of view (with the exception of Fig. 2A-D, as explained in the figure legend). Heatmaps showing maximum amplitude and associated traces of fluorescence over time (Fig. 1) are normalized but not divided by resting light intensity.

Responsive neuron identification

We developed a semi-automated method for objective, reproducible identification of responsive PV interneurons. Supp. Fig. 1 is an extension of Fig. 3 and illustrates this process. The peak fluorescence change from baseline in the 20 msec post-stimulus time window (Fig. 7B) was calculated for each pixel and divided by the pre-stimulus root-mean-square fluorescence during a 20 msec pre-stimulus interval to give the SNR. A SNR cutoff was determined using the pre-stimulus root-mean-square values, and pixels with a response SNR < cutoff were discarded (gray pixels, Supp. Fig. 1A). k-means clustering was then performed on the SNR of the

remaining pixels (Supp. Fig. 1B). This served two main purposes. First, k-means clustering divides pixels into groups likely to contain responsive cells, using the criterion that only pixels with SNR > 5 represent responsive cell bodies (corresponding to yellow, light blue, and medium blue clusters, Supp. Fig. 1B). Second, if multiple pixels represent one cell body, they are likely to have similar SNR values. Because each k-means cluster contains pixels with similar SNRs, two pixels in the same cluster sharing a face are likely to represent the same cell body. This method basically compared each pixel to its neighbors and grouped them based on the likelihood they represent the same cell. One or more contiguous pixels in the same SNR cluster were grouped as one cell if they were no greater than three pixels across, because each pixel measures 6.68 μm, and murine PV interneuron somata are approximately 20 μm in diameter (Kooijmans et al., 2020; Selby et al., 2007; Y. Wang et al., 2002). These criteria excluded some larger clusters of pixels as potentially representing more than one cell even though they had a high SNR. For example, some yellow and orange pixels in Fig. 3C and Supp. Fig. 1A, which correspond with the highest SNR k-means cluster (yellow) in Supp. Fig. 1B, form groups which are larger than 3 pixels across and therefore must contain more than one cell. Likewise, Fig. 2D had fewer identifiable responsive cells that Fig. 2C because Fig 2D had greater overlap. Pixel groups with SNR < 5 or amplitude < 0.001 were excluded and not used to select individual responsive neurons. We also excluded groups of pixels sharing a face to ensure that a single group did not represent multiple cells. The rationale for this grouping procedure is that pixels draw from an area that is smaller than a PV interneuron cell body, and we expect SNR to be uniform over the soma of one neuron. Pixels at a cell edge will not be included due to their lower SNR. Thus, this criterion is conservative in focusing on pixels containing signals arising from distinct, spatially separated neurons.

Experimental design and statistical tests

Further analysis of responses from groups of pixels identified as described above was performed using R and Python. Responses with latency < 1 msec were removed to exclude the effect of direct stimulation; these were generally very close to the stimulation electrode. Responses with latency or time to peak > 13 msec were removed to exclude polysynaptic responses. Disynaptic responses, defined as those occurring more than 2 msec after responses from neighboring cells (< ~ 20 μm) were also excluded. Potential outliers, defined as responses with amplitude, half-width, or latency outside the first or third quartile ± 1.5 * interquartile range, were iteratively identified and visually verified or excluded as appropriate.

Each CV was based on a plot of latency versus distance with at least 8 responsive cells ≥ 100 μm from the stimulating electrode, spanning a range of distances ≥ 100 μm. Analyses included 855 PV interneurons from 59 slices from 13 animals (6 female and 7 male). Relationships between latency and distance were evaluated with linear regression, and p-values were corrected for multiple tests using the false-discovery rate. Euclidean distance was determined between pixels on the 80x80 grid of the CCD-SMQ camera. To determine the appropriate statistical tests, normality was evaluated with a Shapiro-Wilk test, and differences in group variances were evaluated with Levene's tests. CV was normally distributed ($W = 0.9115$, $p = 0.051$). Variance did not differ significantly for male and female animals ($F = 1.2505$, $p = 0.277$), for inter- and intralaminar CV ($F = 0.516$, $p = 0.481$), or for CV directions (intralaminar, L2/3 → L4, L4 → L2/3, L5 → L2/3, L5 → L4; $F = 0.0519$, $p = 0.994$). Therefore, interlaminar versus intralaminar CV, and CV for male versus female animals were compared with t-tests. CV did not differ significantly based on sex ($t = 0.289$, $p = 0.778$). The effect of direction on CV was

455 evaluated with ANOVA followed by post-hoc comparisons using Tukey's honestly significant
456 differences.

457 *Code accessibility*

458 Custom software, R code, and Python code available on request.

459 **References**

460 Adesnik, H. (2018). Layer-specific excitation/inhibition balances during neuronal synchronization in the
461 visual cortex. *J Physiol, 596*(9), 1639-1657. doi:10.1113/JP274986
462 Andermann, M. L., & Moore, C. I. (2006). A somatotopic map of vibrissa motion direction within a
463 barrel column. *Nat Neurosci, 9*(4), 543-551. doi:10.1038/nn1671
464 Bayguinov, P. O., Ma, Y., Gao, Y., Zhao, X., & Jackson, M. B. (2017). Imaging Voltage in Genetically
465 Defined Neuronal Subpopulations with a Cre Recombinase-Targeted Hybrid Voltage Sensor. *J*
466 *Neurosci, 37*(38), 9305-9319. doi:10.1523/JNEUROSCI.1363-17.2017
467 Bradley, J., Luo, R., Otis, T. S., & DiGregorio, D. A. (2009). Submillisecond optical reporting of
468 membrane potential in situ using a neuronal tracer dye. *J Neurosci, 29*(29), 9197-9209.
469 doi:10.1523/JNEUROSCI.1240-09.2009
470 Bruno, R. M., Hahn, T. T., Wallace, D. J., de Kock, C. P., & Sakmann, B. (2009). Sensory experience
471 alters specific branches of individual corticocortical axons during development. *J Neurosci,*
472 *29*(10), 3172-3181. doi:10.1523/JNEUROSCI.5911-08.2009
473 Bucher, D., & Goaillard, J. M. (2011). Beyond faithful conduction: short-term dynamics,
474 neuromodulation, and long-term regulation of spike propagation in the axon. *Prog Neurobiol,*
475 *94*(4), 307-346. doi:10.1016/j.pneurobio.2011.06.001
476 Candy, S. M., & Szatkowski, M. S. (2000). Neuronal excitability and conduction velocity changes in
477 hippocampal slices from streptozotocin-treated diabetic rats. *Brain Res, 863*, 298-301.
478 doi:10.1016/s0006-8993(00)02171-5
479 Cardin, J. A. (2018). Inhibitory Interneurons Regulate Temporal Precision and Correlations in Cortical
480 Circuits. *Trends Neurosci, 41*(10), 689-700. doi:10.1016/j.tins.2018.07.015
481 Chanda, B., Blunck, R., Faria, L. C., Schweizer, F. E., Mody, I., & Bezanilla, F. (2005). A hybrid
482 approach to measuring electrical activity in genetically specified neurons. *Nat Neurosci, 8*(11),
483 1619-1626. doi:10.1038/nn1558
484 Chang, P.-P. (2006). *Heterogeneous spatial patterns of long-term potentiation in hippocampal slices.*
485 University of Wisconsin-Madison, Madison.
486 Chomiak, T., Peters, S., & Hu, B. (2008). Functional architecture and spike timing properties of
487 corticofugal projections from rat ventral temporal cortex. *J Neurophysiol, 100*(1), 327-335.
488 doi:10.1152/jn.90392.2008
489 Compston, A., & Coles, A. (2002). Multiple Sclerosis. *Lancet, 359*, 1221-1231. doi:10.1016/S0140-
490 6736(02)08220-X
491 Corcoba, A., Steullet, P., Duarte, J. M., Van de Looij, Y., Monin, A., Cuenod, M., Gruetter, R., & Do, K.
492 Q. (2015). Glutathione Deficit Affects the Integrity and Function of the Fimbria/Fornix and
493 Anterior Commissure in Mice: Relevance for Schizophrenia. *Int J Neuropsychopharmacol, 19*(3),
494 pyv110. doi:10.1093/ijnp/pyv110
495 Drakesmith, M., Harms, R., Rudrapatna, S. U., Parker, G. D., Evans, C. J., & Jones, D. K. (2019).
496 Estimating axon conduction velocity in vivo from microstructural MRI. *Neuroimage, 203*,
497 116186. doi:10.1016/j.neuroimage.2019.116186

Emmenegger, V., Obien, M. E. J., Franke, F., & Hierlemann, A. (2019). Technologies to Study Action Potential Propagation With a Focus on HD-MEAs. *Front Cell Neurosci, 13*, 159. doi:10.3389/fncel.2019.00159

Feldmeyer, D. (2012). Excitatory neuronal connectivity in the barrel cortex. *Front Neuroanat, 6*, 24. doi:10.3389/fnana.2012.00024

Ferguson, B. R., & Gao, W. J. (2018). PV Interneurons: Critical Regulators of E/I Balance for Prefrontal Cortex-Dependent Behavior and Psychiatric Disorders. *Front Neural Circuits, 12*, 37. doi:10.3389/fncir.2018.00037

Fields, R. D. (2015). A new mechanism of nervous system plasticity: activity-dependent myelination. *Nat Rev Neurosci, 16*(12), 756-767. doi:10.1038/nrn4023

Fukuda, T., & Kosaka, T. (2003). Ultrastructural study of gap junctions between dendrites of parvalbumin-containing GABAergic neurons in various neocortical areas of the adult rat. *Neuroscience, 120*(1), 5-20. doi:10.1016/s0306-4522(03)00328-2

Galarreta, M., & Hestrin, S. (2002). Electrical and chemical synapses among parvalbumin fast-spiking GABAergic interneurons in adult mouse neocortex. *PNAS, 99*, 12438-12443. doi:10.1073/pnas.192159599

Gandal, M. J., Edgar, J. C., Klook, K., & Siegel, S. J. (2012). Gamma synchrony: towards a translational biomarker for the treatment-resistant symptoms of schizophrenia. *Neuropharmacology, 62*(3), 1504-1518. doi:10.1016/j.neuropharm.2011.02.007

Ghitani, N., Bayguinov, P. O., Ma, Y., & Jackson, M. B. (2015). Single-trial imaging of spikes and synaptic potentials in single neurons in brain slices with genetically encoded hybrid voltage sensor. *J Neurophysiol, 113*(4), 1249-1259. doi:10.1152/jn.00691.2014

Gilbert, C. D. (1992). Horizontal Integration and Cortical Dynamics. *Neuron, 9*, 1-13. doi:10.1016/0896-6273(92)90215-y

Gloveli, T., Dugladze, T., Saha, S., Monyer, H., Heinemann, U., Traub, R. D., Whittington, M. A., & Buhl, E. H. (2005). Differential involvement of oriens/pyramidale interneurones in hippocampal network oscillations in vitro. *J Physiol, 562*(Pt 1), 131-147. doi:10.1113/jphysiol.2004.073007

Gonzalez-Burgos, G., Cho, R. Y., & Lewis, D. A. (2015). Alterations in cortical network oscillations and parvalbumin neurons in schizophrenia. *Biol Psychiatry, 77*(12), 1031-1040. doi:10.1016/j.biopsych.2015.03.010

Gottlieb, J. P., & Keller, A. (1997). Intrinsic circuitry and physiological properties of pyramidal neurons in rat barrel cortex. *Exp Brain Res, 115*, 47-60. doi:10.1007/pl00005684

Grinvald, A., Ross, W. N., & Farber, I. (1981). Simultaneous optical measurements of electrical activity from multiple sites on processes of cultured neurons. *Proc Natl Acad Sci U S A, 78*. doi:10.1073/pnas.78.5.3245

Hamada, M. S., Popovic, M. A., & Kole, M. H. (2017). Loss of Saltation and Presynaptic Action Potential Failure in Demyelinated Axons. *Front Cell Neurosci, 11*, 45. doi:10.3389/fncel.2017.00045

Helmstaedter, M., Staiger, J. F., Sakmann, B., & Feldmeyer, D. (2008). Efficient recruitment of layer 2/3 interneurons by layer 4 input in single columns of rat somatosensory cortex. *J Neurosci, 28*(33), 8273-8284. doi:10.1523/JNEUROSCI.5701-07.2008

Ivanov, V., Polykretis, I. F., & Michmizos, K. P. (2019). *Axonal Conduction Velocity Impacts Neuronal Network Oscillations*. Paper presented at the 2019 IEEE EMBS International Conference on Biomedical & Health Informatics (BHI).

Keller, A., & Asanuma, H. (1993). Synaptic Relationships Involving Local Axon Collaterals of Pyramidal Neurons in Cat Motor Cortex. *J Comp Neurol, 336*, 229-242. doi:10.1002/cne.903360206

Kim, J. H., Renden, R., & von Gersdorff, H. (2013). Dysmyelination of auditory afferent axons increases the jitter of action potential timing during high-frequency firing. *J Neurosci, 33*(22), 9402-9407. doi:10.1523/JNEUROSCI.3389-12.2013

Kimura, F., Itami, C., Ikezoe, K., Tamura, H., Fujita, I., Yanagawa, Y., Obata, K., & Ohshima, M. (2010). Fast activation of feedforward inhibitory neurons from thalamic input and its relevance to the

549 regulation of spike sequences in the barrel cortex. *J Physiol, 588*(Pt 15), 2769-2787.
550 doi:10.1113/jphysiol.2010.188177
551 Kooijmans, R. N., Sierhuis, W., Self, M. W., & Roelfsema, P. R. (2020). A Quantitative Comparison of
552 Inhibitory Interneuron Size and Distribution between Mouse and Macaque V1, Using Calcium-
553 Binding Proteins. *Cereb Cortex Commun, 1*(1), tgaa068. doi:10.1093/texcom/tgaa068
554 Kremer, Y., Leger, J. F., Goodman, D., Brette, R., & Bourdieu, L. (2011). Late emergence of the vibrissa
555 direction selectivity map in the rat barrel cortex. *J Neurosci, 31*(29), 10689-10700.
556 doi:10.1523/JNEUROSCI.6541-10.2011
557 Kress, G. J., & Mennerick, S. (2009). Action potential initiation and propagation: upstream influences on
558 neurotransmission. *Neuroscience, 158*(1), 211-222. doi:10.1016/j.neuroscience.2008.03.021
559 Larsen, D. D., & Callaway, E. M. (2006). Development of layer-specific axonal arborizations in mouse
560 primary somatosensory cortex. *J Comp Neurol, 494*(3), 398-414. doi:10.1002/cne.20754
561 Lauber, E., Filice, F., & Schwaller, B. (2018). Parvalbumin neurons as a hub in autism spectrum
562 disorders. *J Neurosci Res, 96*(3), 360-361. doi:10.1002/jnr.24204
563 Lee, J. A., Miao, Z., Chen, Q. Y., Li, X. H., & Zhuo, M. (2021). Multiple synaptic connections into a
564 single cortical pyramidal cell or interneuron in the anterior cingulate cortex of adult mice. *Mol*
565 *Brain, 14*(1), 88. doi:10.1186/s13041-021-00793-8
566 Liu, Wang, H. G., Pitt, G. S., & Liu, Z. J. (2022). Direct Observation of Compartment-Specific
567 Localization and Dynamics of Voltage-Gated Sodium Channels. *J Neurosci, 42*(28), 5482-5498.
568 doi:10.1523/JNEUROSCI.0086-22.2022
569 Liu, T. Y., Hsieh, J. C., Chen, Y. S., Tu, P. C., Su, T. P., & Chen, L. F. (2012). Different patterns of
570 abnormal gamma oscillatory activity in unipolar and bipolar disorder patients during an implicit
571 emotion task. *Neuropsychologia, 50*(7), 1514-1520. doi:10.1016/j.neuropsychologia.2012.03.004
572 Ma, Y., Bayguinov, P. O., & Jackson, M. B. (2017). Action Potential Dynamics in Fine Axons Probed
573 with an Axonally Targeted Optical Voltage Sensor. *eNeuro, 4*(4), 0146-0147.
574 doi:10.1523/ENEURO.0146-17.2017
575 Ma, Y., Bayguinov, P. O., & Jackson, M. B. (2019). Optical Studies of Action Potential Dynamics with
576 hVOS probes. *Curr Opin Biomed Eng, 12*, 51-58. doi:10.1016/j.cobme.2019.09.007
577 McDougall, S., Vargas Riad, W., Silva-Gotay, A., Tavares, E. R., Harpalani, D., Li, G. L., & Richardson,
578 H. N. (2018). Myelination of Axons Corresponds with Faster Transmission Speed in the
579 Prefrontal Cortex of Developing Male Rats. *eNeuro, 5*(4), 0203-0218.
580 doi:10.1523/ENEURO.0203-18.2018
581 McGuire, B. A., Gilbert, C. D., Rivlin, P. K., & Wiesel, T. N. (1991). Targets of Horziontal Connections
582 in Macaque Primary Visual Cortex. *J Comp Neurol, 305*(3), 370-392.
583 doi:10.1002/cne.903050303
584 Murakoshi, T., Guo, J., & Ichinose, T. (1993). Electrophysiological identification of horizontal synaptic
585 connections in rat visual cortex in vitro. *Neurosci Lett, 163*(2), 211-214. doi:10.1016/0304-
586 3940(93)90385-x
587 Narayanan, R. T., Egger, R., Johnson, A. S., Mansvelder, H. D., Sakmann, B., de Kock, C. P., &
588 Oberlaender, M. (2015). Beyond Columnar Organization: Cell Type- and Target Layer-Specific
589 Principles of Horizontal Axon Projection Patterns in Rat Vibrissal Cortex. *Cereb Cortex, 25*(11),
590 4450-4468. doi:10.1093/cercor/bhv053
591 Nave, K. A. (2010). Myelination and support of axonal integrity by glia. *Nature, 468*(7321), 244-252.
592 doi:10.1038/nature09614
593 Olmos-Serrano, J. L., Kang, H. J., Tyler, W. A., Silbereis, J. C., Cheng, F., Zhu, Y., Pletikos, M.,
594 Jankovic-Rapan, L., Cramer, N. P., Galdzicki, Z., Goodliffe, J., Peters, A., Sethares, C., Delalle,
595 I., Golden, J. A., Haydar, T. F., & Sestan, N. (2016). Down Syndrome Developmental Brain
596 Transcriptome Reveals Defective Oligodendrocyte Differentiation and Myelination. *Neuron,*
597 *89*(6), 1208-1222. doi:10.1016/j.neuron.2016.01.042
598 Pajevic, S., Basser, P. J., & Fields, R. D. (2014). Role of myelin plasticity in oscillations and synchrony
599 of neuronal activity. *Neuroscience, 276*, 135-147. doi:10.1016/j.neuroscience.2013.11.007

Palmer, L. M., & Stuart, G. J. (2006). Site of action potential initiation in layer 5 pyramidal neurons. *J Neurosci, 26*(6), 1854-1863. doi:10.1523/JNEUROSCI.4812-05.2006

Panzera, L. C., & Hoppa, M. B. (2019). Genetically Encoded Voltage Indicators Are Illuminating Subcellular Physiology of the Axon. *Front Cell Neurosci, 13*, 52. doi:10.3389/fncel.2019.00052

Pedroni, A., Minh do, D., Mallamaci, A., & Cherubini, E. (2014). Electrophysiological characterization of granule cells in the dentate gyrus immediately after birth. *Front Cell Neurosci, 8*, 44. doi:10.3389/fncel.2014.00044

Petersen, C. C. H., Grinvald, A., & Sakmann, B. (2003). Spatiotemporal Dynamics of Sensory Responses in Layer 2/3 of Rat Barrel Cortex Measured In Vivo by Voltage-Sensitive Dye Imaging Combined with Whole-Cell Voltage Recordings and Neuron Reconstructions. *J Neurosci, 23*(4), 1298-1309. doi:10.1523/JNEUROSCI.23-04-01298.2003

Popovic, M. A., Foust, A. J., McCormick, D. A., & Zecevic, D. (2011). The spatio-temporal characteristics of action potential initiation in layer 5 pyramidal neurons: a voltage imaging study. *J Physiol, 589*(17), 4167-4187. doi:10.1113/jphysiol.2011.209015

Pouille, F., & Scanziani, M. (2001). Enforcement of temporal fidelity in pyramidal cells by somatic feed-forward inhibition. *Science, 293*(5532), 1159-1163. doi:10.1126/science.1060342

Radivojevic, M., Franke, F., Altermatt, M., Muller, J., Hierlemann, A., & Bakkum, D. J. (2017). Tracking individual action potentials throughout mammalian axonal arbors. *Elife, 6*. doi:10.7554/eLife.30198

Roy, K., Murtie, J. C., El-Khodor, B. F., Edgar, N., Sardi, S. P., Hooks, B. M., Benoit-Marand, M., Chen, C., Moore, H., O'Donnell, P., Brunner, D., & Corfas, G. (2007). Loss of erbB signaling in oligodendrocytes alters myelin and dopaminergic function, a potential mechanism for neuropsychiatric disorders. *PNAS, 104*(19), 8131-8136. doi:10.1073/pnas.0702157104

Sakai, T., Komuro, H., Katoh, Y., Sasaki, H., Momose-Sato, Y., & Kamino, K. (1991). Optical Determination of Impulsive Conduction Velocity During Development of Embryonic chick Cervical Vagus Nerve Bundles. *J Physiol, 439*, 361-381. doi:10.1113/jphysiol.1991.sp018671

Salami, M., Itami, C., Tsumoto, T., & Kimura, F. (2003). Change of conduction velocity by regional myelination yields constant latency irrespective of distance between thalamus and cortex. *PNAS, 100*(10), 6174-6179. doi:10.1073/pnas.0937380100

Salami, M., Kimura, F., & Tsumoto, T. (2003). Postnatal Changes of Conduction Velocity of the Fibers in and out of the Mouse Barrel Cortex. *Iran Biomed J, 7*(2), 57-63.

Schubert, D., Kotter, R., Luhmann, H. J., & Staiger, J. F. (2006). Morphology, electrophysiology and functional input connectivity of pyramidal neurons characterizes a genuine layer va in the primary somatosensory cortex. *Cereb Cortex, 16*(2), 223-236. doi:10.1093/cercor/bhi100

Schubert, D., Staiger, J. F., Cho, N., Kotter, R., Zilles, K., & Luhmann, H. J. (2001). Layer-Specific Intracolumnar and Transcolumnar Functional Connectivity of Layer V Pyramidal Cells in Rat Barrel Cortex. *J Neurosci, 21*(10), 3580-3592. doi:10.1523/JNEUROSCI.21-10-03580.2001

Selby, L., Zhang, C., & Sun, Q. Q. (2007). Major defects in neocortical GABAergic inhibitory circuits in mice lacking the fragile X mental retardation protein. *Neurosci Lett, 412*(3), 227-232. doi:10.1016/j.neulet.2006.11.062

Shlosberg, D., Abu-Ghanem, Y., & Amitai, Y. (2008). Comparative properties of excitatory and inhibitory inter-laminar neocortical axons. *Neuroscience, 155*(2), 366-373. doi:10.1016/j.neuroscience.2008.06.003

Shu, Y., Duque, A., Yu, Y., Haider, B., & McCormick, D. A. (2007). Properties of action-potential initiation in neocortical pyramidal cells: evidence from whole cell axon recordings. *J Neurophysiol, 97*(1), 746-760. doi:10.1152/jn.00922.2006

Soleng, A. F., Raastad, M., & Andersen, P. (2003). Conduction latency along CA3 hippocampal axons from rat. *Hippocampus, 13*(8), 953-961. doi:10.1002/hipo.10141

Staiger, J. F., & Petersen, C. C. H. (2021). Neuronal Circuits in Barrel Cortex for Whisker Sensory Perception. *Physiol Rev, 101*(1), 353-415. doi:10.1152/physrev.00019.2019

650 Telfeian, A. E., & Connors, B. W. (2003). Widely integrative properties of layer 5 pyramidal cells support
651 a role for processing of extralaminar synaptic inputs in rat neocortex. *Neuroscience Letters,*
652 *343*(2), 121-124. doi:10.1016/s0304-3940(03)00379-3
653 Thomson, A. M., West, D. C., Wang, Y., & Bannister, A. P. (2002). Synaptic Connections and Small
654 Circuits Involving Excitatory and Inhibitory Neurons in Layers 2-5 of Adult Rat and Cat
655 Neocortex: Triple Intracellular Recordings and Biocytin Labelling In Vitro. *Cereb Cortex, 12*(9),
656 936-953. doi:10.1093/cercor/12.9.936
657 Vacher, H., Mohapatra, D. P., & Trimmer, J. S. (2008). Localization and targeting of voltage-dependent
658 ion channels in mammalian central neurons. *Physiol Rev, 88*(4), 1407-1447.
659 doi:10.1152/physrev.00002.2008
660 Vecchia, D., Beltramo, R., Vallone, F., Chereau, R., Forli, A., Molano-Mazon, M., Bawa, T., Binini, N.,
661 Moretti, C., Holtmaat, A., Panzeri, S., & Fellin, T. (2020). Temporal Sharpening of Sensory
662 Responses by Layer V in the Mouse Primary Somatosensory Cortex. *Curr Biol, 30*(9), 1589-1599
663 e1510. doi:10.1016/j.cub.2020.02.004
664 Wang, Zhang, Z., Chanda, B., & Jackson, M. B. (2010). Improved probes for hybrid voltage sensor
665 imaging. *Biophys J, 99*(7), 2355-2365. doi:10.1016/j.bpj.2010.07.037
666 Wang, Y., Gupta, A., Toledo-Rodriguez, M., Wu, C. Z., & Markram, H. (2002). Anatomical,
667 Physiological, Molecular and Circuit Properties of Nest Basket Cells in the Developing
668 Somatosensory Cortex. *Cereb Cortex, 12*(4), 395-410. doi:10.1093/cercor/12.4.395
669 Woolsey, T. A., & Van der Loos, H. (1970). The Structural Organization of Layer IV in the
670 Somatosensory Region (S1) of Mouse Cerebral Cortex. *Brain Res, 17*(2), 205-242.
671 doi:10.1016/0006-8993(70)90079-x
672 Xu, X., Olivas, N. D., Ikrar, T., Peng, T., Holmes, T. C., Nie, Q., & Shi, Y. (2016). Primary visual cortex
673 shows laminar-specific and balanced circuit organization of excitatory and inhibitory synaptic
674 connectivity. *J Physiol, 594*(7), 1891-1910. doi:10.1113/JP271891

675